A multiplexed optofluidic biomolecular sensor for low mass detection†

Sudeep Mandal,‡[a] Julie M. Goddard‡[b] and David Erickson*[b]

Received 20th April 2009, Accepted 29th June 2009
First published as an Advance Article on the web 11th July 2009
DOI: 10.1039/b907826f

Optical techniques have proven to be well suited for *in situ* biomolecular sensing because they enable high fidelity measurements in aqueous environments, are minimally affected by background solution pH or ionic strength, and facilitate label-free detection. Recently, there has been significant interest in developing new classes of optically resonant biosensors possessing very high quality-factors. This high quality-factor enables them to resolve the presence of very small amounts of bound mass and leads to very low limits of detection. A drawback of these devices is that the majority of the resonant electromagnetic energy is confined within the solid light-guiding structure thus limiting the degree to which it overlaps with the bound matter. This in turn lowers the ultimate device sensitivity, or the change in output signal in response to changes in bound mass. Here we present a novel optofluidic biosensor platform that incorporates a unique one-dimensional photonic crystal resonator array which enables significantly stronger light-matter interaction. We show here how this, coupled with the ability of planar photonic crystals to spatially localize the optical field to mode volumes on the order of a wavelength cubed, enables a limit of detection on the order of 63 ag total bound mass (estimated using a polyelectrolyte growth model) and a device sensitivity an order of magnitude better than similar devices. The multiplexing capabilities of our sensor are demonstrated by the individual and concurrent detection of interleukins 4, 6 and 8 using a sandwich assay.

Introduction

Biosensors that exploit optical,[1–3] electrical,[4] and mechanical[5] methods of signal transduction bypass the need for fluorescent, radio, or enzymatic labels. Label-free approaches can exhibit enhanced sensitivity and specificity over traditional sensors because such labels can: interfere with the binding event, non-specifically adsorb to the surface, and complicate the chemistry of the detection reaction.[6] Of these methods, optical biosensors are particularly promising because of their low limits of detection, high sensitivities and capacity for multiplexed detection.[7–9] While recent nano-mechanical[10] and nano-electrical[11,12] devices have similarly proven successful, they tend to be limited in that they require measurements to be made outside of the liquid environment, or exhibit sensitivity to background electrical conditions such as solution pH and ionic strength. The performance of optical sensors is far less dependent on favourable environmental conditions making them appropriate for a much broader range of applications.

This advantage, amongst others, has led to the development of a large number of label-free optical sensor technologies, including interferometric,[13,14] resonant-cavity,[3,15,16] photonic crystal[17–19] and surface plasmon resonance (SPR)[20–22] devices. The performance of a biosensor is characterized by two parameters: its limit of detection (the smallest amount or target that can be detected) and the device sensitivity (or the amount by which the detection signal responds to a change in input). In the case of optical biosensors the limit of detection is largely determined by how precisely a change in the output signal can be resolved and sensitivity by how strong the overlap is between the electromagnetic energy[23] and the target molecules. As a result of this, there has been significant recent interest in the development of whispering gallery mode (WGM) type biosensors, exploiting toroidal,[24] microsphere,[25] microring,[26] and microdisk[27] resonator structures. The advantage of these devices is the high degree to which electromagnetic energy can be localized resulting in very high quality factors (Q-factor) and very narrow line-widths. These narrow line widths make it relatively simple to resolve subtle changes in the resonant frequency, yielding very low limits of detection.[3] In general however to achieve these high Q-factors the electromagnetic energy must be largely confined within a solid structure and thus the extent to which it can interact with the bound molecular targets is limited to a small portion of the evanescent field, negatively impacting device sensitivity.

We present here a label-free multiplexed immunosensor based on our nanoscale optofluidic sensor array (NOSA) architecture.[28] Illustrated in Fig. 1, our device consists of arrays of evanescently coupled one-dimensional photonic crystal resonators. As we demonstrate below, the accessible optical field inside the holes of photonic crystal is significantly

---

[a] *School of Applied and Engineering Physics, Cornell University, Ithaca, NY, 14853, USA*
[b] *Sibley School of Mechanical and Aerospace Engineering, Cornell University, Ithaca, NY, 14853, USA. E-mail: de54@cornell.edu; Fax: +1 607-255-1222; Tel: +1 607-255-4861*

† Electronic supplementary information (ESI) available: Schematic of surface functionalization chemistry (Fig. S1), plot showing the resulting spectra from multiplexed assays after introduction of 10 μg/ml of (a) interleukin 6, (b) interleukin 8, and (c) interleukin 4, followed by association with secondary antibody (Fig. S2), NOSA chip integrated with PDMS microfluidics and secured in a plexiglass housing (Fig. S3), effect of blocking buffer on device performance (Fig. S4). See DOI: 10.1039/b907826f

‡ S.M. and J.M.G. contributed equally to this work.

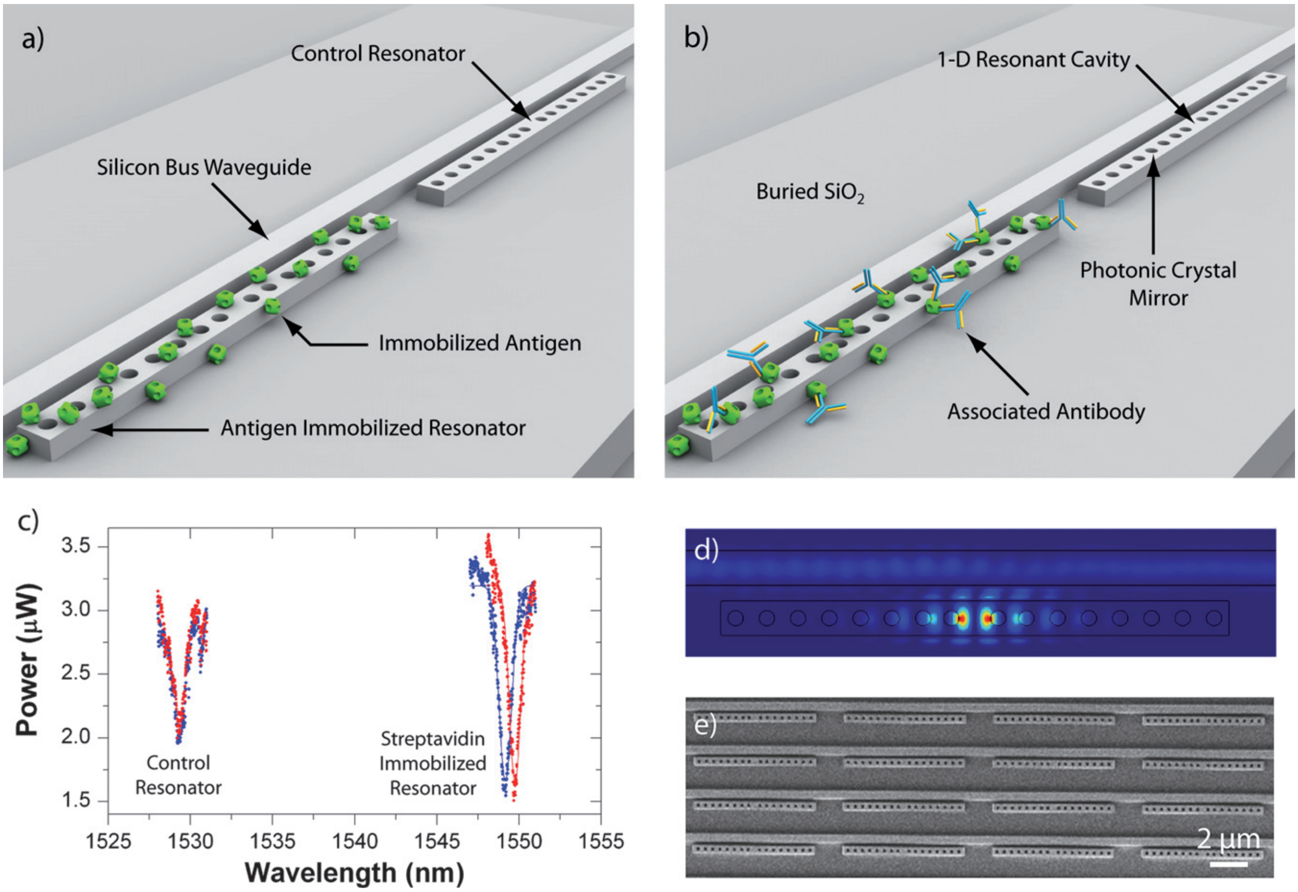

Fig. 1 Nanoscale Optofluidic Sensor Arrays. (a) 3D rendering of the NOSA device showing two 1-D photonic crystal resonators evanescently coupled to a silicon bus waveguide. The first resonator is immobilized with an antigen whereas the second resonator acts as a control. (b) 3D rendering illustrating the association of the corresponding antibody to the antigen immobilized resonator (not drawn to scale). (c) Experimental data illustrating the successful detection of 45 μg/ml of anti-streptavidin antibody. The blue trace shows the initial baseline spectrum corresponding to Figure 1a where the first resonator is immobilized with streptavidin. The red trace shows the test spectra after the association of anti-streptavidin as shown in Figure 1b. The resonant wavelength of the control is unchanged while that of the streptavidin immobilized resonator red-shifts appreciably indicating successful detection of anti-streptavidin. (d) Finite difference time domain (FDTD) simulation of the steady state electric field distribution within the 1-D photonic crystal resonator at the resonant wavelength. (e) SEM image demonstrating the 2-dimensional multiplexing capability of the NOSA architecture.

stronger than the evanescent fields of WGM sensors, thereby strengthening the light-matter interactions that enhance sensitivity. We demonstrate here how this coupled with the ability of planar photonic crystals to spatially localize the optical field to mode volumes on the order of a wavelength cubed,[29,30] enables a limit of detection on the order of 10s of attograms total bound mass (compared with femtograms[17,31,32]) and a device sensitivity an order of magnitude better than similar devices. In this paper we characterize the sensitivity of our device to bound mass by monitoring the growth of a polyelectrolyte multilayer and the resulting change in resonant wavelength. Real-time binding kinetics and dynamic range are determined by associating anti-streptavidin with surface-immobilized streptavidin. While many optically resonant sensors face design challenges when moving towards performing highly multiplexed detection, we demonstrate the facile multiplexability our approach affords through the concurrent detection of multiple interleukins (IL-4, IL-6, and IL-8) in a single integrated optofluidic[33,34] device.

Results

Device operation and detection principle

As shown in Fig. 1, the NOSA platform consists of multiple evanescently coupled 1-D photonic crystal resonators situated along a single bus waveguide. A central cavity in the 1-D photonic crystal structure of each resonator gives rise to a defect state[35] in the photonic bandgap. This results in a resonant dip in the output spectrum of the bus waveguide. By tailoring the cavity length, each of the evanescently coupled 1-D resonators is designed to possess a unique resonant wavelength. Fig. 1d illustrates the steady-state electric field intensity distribution within the 1-D resonator at the resonant wavelength. The binding of target biomolecules to the surface of the resonator induces a slight increase in the local refractive index around it. The interaction of the resonant optical field with the bound target biomolecules at the sensor surface and within the photonic crystal holes results in a red-shift in the corresponding resonant wavelength of the resonator. Put simply, the increase in the refractive index of the optical cavity caused by the presence of bound mass increases the effective optical length of the cavity and thereby the wavelength of light that will resonate within it. The output optical spectrum from the bus waveguide can be constantly monitored and binding of target biomolecules to the resonator is inferred when a red-shift is observed. Fig. 1c illustrates a typical experiment demonstrating the detection of anti-streptavidin antibody binding to a streptavidin functionalized resonator. Note that no observable shift is detected in the case of the control resonator which is not streptavidin functionalized.

Since each evanescently coupled 1-D resonator possesses a unique resonance in the output spectrum, multiplexed detection along a single waveguide is possible. In this case, each of the 1-D resonators is initially functionalized with a unique capture molecule. The sample containing target bio-molecules is made to flow over the 1-D resonators while the output spectrum is monitored. By observing the combination of resonances that red-shift it is possible to determine which target molecules were present in the detection sample. Analysis of the degree of red-shift provides quantitative information regarding the amount of bound mass which can be correlated to concentration of target molecule present in a sample. Fig. 1e is an SEM image of a NOSA array, illustrating the 2-dimensional multiplexing capabilities of the platform.

Device characterization

To quantitatively determine the device sensitivity to bound mass, we use a polyelectrolyte multilayer "layer-by-layer" deposition technique. This technique enables an accurate determination of the sensing range of a biosensor, *i.e.*, how far above the sensor surface can biomolecules bind and still produce a shift in the resonant wavelength. This is important to characterize as it helps determine what kinds of surface conjugation techniques can be used successfully to immobilize the required capture biomolecules without pushing the bound target biomolecules too far above the sensor surface and away from the sensing region. Briefly, multilayers of polyethyleneimine and polyacrylic acid were deposited on the glutaraldehyde functionalized NOSA device, and on similarly functionalized silicon wafers in parallel. The scheme for surface functionalization is illustrated in Figure S1 (see ESI†) and is fully described in the methods section. After deposition of each layer, output spectra were recorded to quantify shift in resonant wavelengths and polyelectrolyte multilayer film thickness was determined on silicon wafers using ellipsometry. Output spectra were compared to the initial baseline spectra to determine resonance shift ($\Delta\lambda$, in nm), and were plotted against film thickness as plotted in Fig. 2.

Baseline spectra ($\Delta\lambda = 0$ nm) were taken on 5 NOSA resonators and parallel silicon wafers after surface functionalization. A film thickness of 3.11 nm corresponds to the molecular thickness of native oxide, amine-terminated silane monolayer, and glutaraldehyde functionalization, each of which contributes $\sim$1 nm to total film thickness. Since the field at the sensor surface exhibits an exponential decay, the growth of the polyelectrolyte multilayer and the resulting effect on resonance shift were fit to an exponential model as shown in Fig. 2. Although the device continues to respond past 30 nm of deposited polyelectrolyte multilayers, it exhibits the greatest sensitivity in the first 20 nm of multilayer growth, with an apparent sensitivity of 0.35 nm resonance shift per nanometer multilayer growth. This suggests that the NOSA device is well suited for small molecule detection, as the Stokes radii of proteins relevant in medical diagnostics and nucleic acids relevant in pathogen detection tend to be below 15 nm, in the region of greatest device sensitivity. Fig. 3 is a finite difference time domain (FDTD) simulation that illustrates the field decay within the innermost hole of the 1-D resonator which reaches a 1/e value 80 nm away from the hole surface. Thus the NOSA architecture can probe regions even 80–90 nm away from

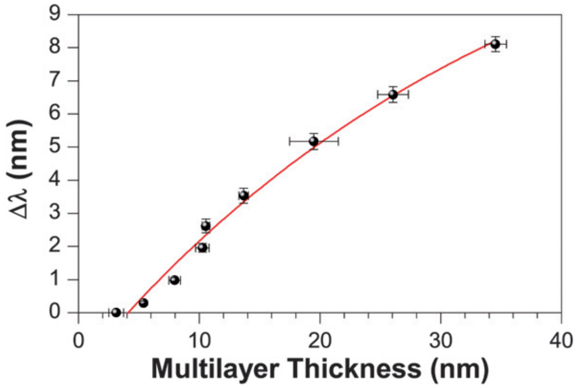

Fig. 2 Optical response to polyelectrolyte layer growth. Effect of polyelectrolyte multilayer thickness on resonance shift. Data have been fit to an exponential model; error bars represent standard deviation.

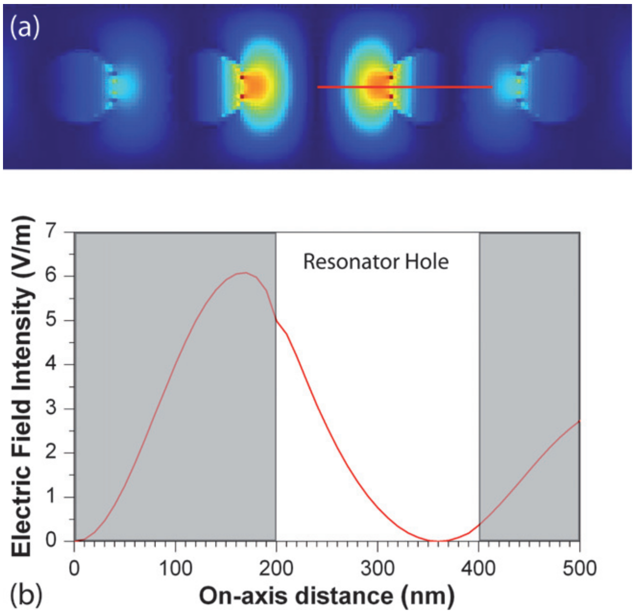

Fig. 3 Electric field distribution inside resonator hole. (a) FDTD simulation showing the steady state electric field distribution within the central resonator cavity for the resonant wavelength. (b) Plot of the Electric field intensity along the red line shown in Figure 3a. The gray boxes indicate the device silicon whereas the white area indicates the electric field intensity within the innermost hole of the 1-D resonator. It is clear that a significant portion of the resonant field extends within the holes of the resonator thus allowing for strong light-matter interactions within the holes. The field decays to its 1/e value approximately 80 nm away from the wall of the hole.

the substrate, which is consistent with our experimental observation (Fig. 2) that the red-shift did not saturate for polyelectrolyte layers up to 35 nm thick.

Label-free multiplexed immunoassay

Cytokines represent a unique class of serum signaling proteins that have proven to be a useful tool in diagnostics. Specifically, interleukins have been demonstrated to be excellent candidates as cancer biomarkers.[36] The potential for monitoring of *in-vivo* concentrations of various interleukins for prognosis in cancer patients[37,38] has generated significant interest in the biosensor community.

To demonstrate the multiplexability of the NOSA device, monoclonal antibodies to interleukin 4, 6, and 8 were immobilized on adjacent resonators and tested for cross-reactivity (see methods). Glutaraldehyde functionalized resonators and streptavidin immobilized resonators served as controls for non-specific analyte adsorption. As an additional control, cross-reactivity of secondary antibodies with complementary as well as non-complementary capture antibodies was assessed. Resonance shifts due to cross-reactivity were less than 0.02 nm in all experiments and did not therefore significantly affect the detection resonance shift. The Q-factor of 3000 for our resonators sets our detection limit at 0.01 nm. Reported data are representative of experiments repeated on at least two separate days. To assess multiplex capability, we tested concurrent detection of multiple interleukins after their association with secondary interleukin antibodies. Fig. 4a shows the resulting spectra after introducing 1 μg/ml of interleukin 8 along with 10 μg/ml of interleukin 6, followed by sequential association of secondary antibodies corresponding to each of these interleukins. In the figure, the resonant wavelengths numbered 1 through 5 correspond to control (glutaraldehyde functionalized), streptavidin-functionalized control, anti-interleukin 6, anti-interleukin 4, and anti-interleukin 8, respectively (Fig. 4b). The test spectrum (red) is superimposed over the baseline spectrum (blue) to illustrate the lack of significant non-specific binding. We observe shifts in the resonance corresponding to immobilized monoclonal anti-interleukin 8 (0.58 nm) and 6 (0.68 nm), but no significant shift in the resonance corresponding to immobilized monoclonal anti-interleukin 4. This further supports the ability of the NOSA device to function as a multiplexed biosensor with little cross-reactivity or non-specific binding. Figure S2 (see ESI†) shows the resulting spectra from other multiplexed assays after introduction of 10 μg/ml of interleukin 6, 8, or 4 (respectively), followed by association with secondary antibody. In each case, there is an average shift of 0.72 nm (mean of 6 determinations) with a standard deviation of 0.1 nm in the resonant wavelength corresponding to the target analyte used in a given experiment.

Physiologically relevant concentrations of serum interleukins for *in-vivo* monitoring are on the order of 1–10 pg/ml, which is within the detection limits of available ELISA techniques.[39,40] While the demonstrated LOD of the NOSA prevents the detection of interleukins at these concentrations, as outlined in the subsequent section, improvements in the sensor design can enable extremely high-Q microcavity resonators with a significantly improved detection limit. In addition, by tagging the secondary antibodies with nanoparticles possessing a high refractive (such as titanium dioxide) the induced red-shift can be amplified thus offering another means for enhancing the sensitivity of this biosensor platform. In its current design, our device can detect antibodies in a concentration range of 1 μg/ml to 1 mg/ml, which is of clinical significance in medical diagnostics (*i.e.* HIV detection), and drug screening.[41]

Determination of dynamic range

A dose-response curve was generated by associating varying concentrations of anti-streptavidin antibody to immobilized streptavidin. Since all antibodies possess roughly the same size and molecular weight, we utilize an antibody-antigen system for determining and comparing the dynamic range of our NOSA sensor. Antibody concentration was varied from 0.010 to

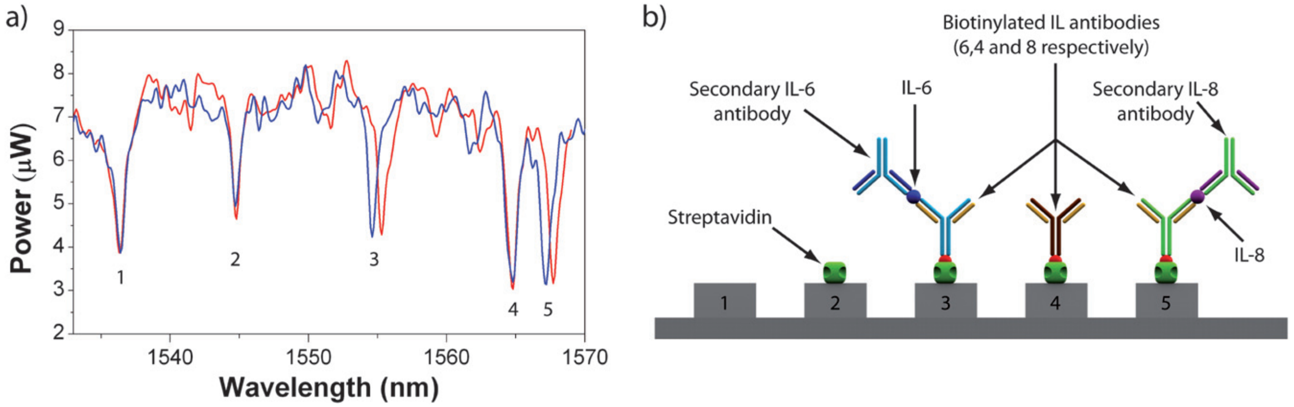

Fig. 4 Multipexed detection of interleukins. (a) Spectra for resonators labelled 1 through 5 that correspond to control (glutaraldehyde functionalized), streptavidin-functionalized control, anti-interleukin 6, anti-interleukin 4, and anti-interleukin 8, respectively. The trace in blue shows the initial baseline spectrum. The red trace corresponds to the test spectrum after introducing 10 μg/ml of interleukin 6 along with 1 μg/ml of interleukin 8, followed by the sequential association of secondary antibodies corresponding to each of these interleukins. We clearly see shifts corresponding to the resonators functionalized with anti-interleukin 6 and 8 (Resonance 3 and 5 respectively) while the other resonances do not shift appreciably thus indicating the lack of non-specific binding. Fabry-Perot resonances were filtered out in both spectra by performing a fast Fourier transform. (b) Reaction stages at each of 5 resonators.

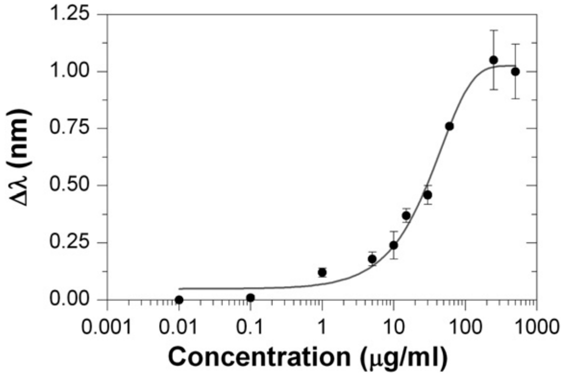

Fig. 5 Streptavidin/anti-streptavidin dose response curve. Data have been fit to a sigmoidal model; error bars represent standard deviation.

500 μg/ml, and the resulting shift in resonant wavelength was recorded. The data were plotted on a log-linear scale as shown in Fig. 5, and fitted to a sigmoidal[42] dose response model. These data indicate that the NOSA is capable of quantifying the concentration of antibody present in a sample in a dynamic range spanning two orders of magnitude (1 to 100 μg/ml) which is comparable to previous work on a streptavidin anti-streptavidin sensor.[43] Using different biomolecular systems, WGM sensors[3,44] have previously demonstrated dynamic ranges spanning seven to eight orders of magnitude. As discussed in the next section, our current experiments are less sensitive due to the lower Q-factor of the 1-D resonators in comparison to most WGM sensors. However, this is not a fundamental limit and with future work on fabricating high-Q 1-D photonic crystal resonators, it should be possible to achieve similar dynamic ranges due to the enhanced detection limit while retaining the small device footprint and easy multiplexability afforded by the NOSA architecture.

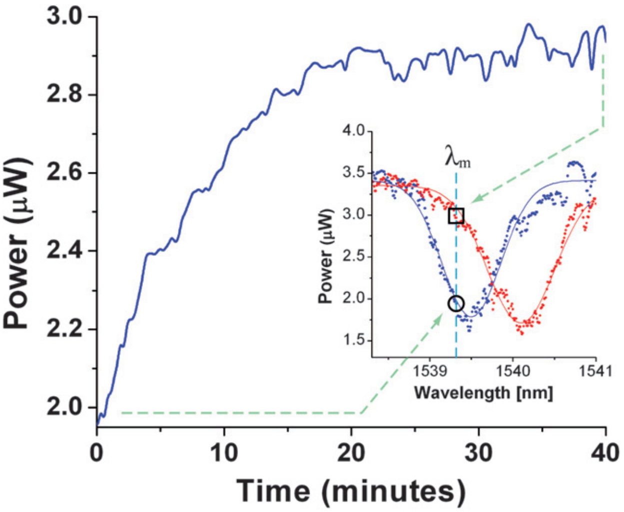

Fig. 6 Measurement of binding kinetics. Trace of recorded power at a fixed wavelength λ_m as a function of time during the association of 45 μg/ml of anti-streptavidin antibody to a streptavidin functionalized resonator which clearly shows the reaction proceeding to saturation. The inset shows the correspondence of points at the start and end of the trace to the initial baseline and final red-shifted resonant spectrum.

Instead of continuously tuning the laser across its operational range to record the output spectrum, it is also possible to monitor the output power at a fixed wavelength along the sloping profile of a resonant dip in the spectrum. As the resonant dip red-shifts due to the binding of target biomolecules, the power recorded at this fixed wavelength is observed to correspondingly increase as a function of time. Much like SPR sensors, it is possible to monitor biomolecular interactions in real-time and perform binding kinetic studies using this platform. Fig. 6 shows the output power at a fixed wavelength (λ_m) for the association of 45 μg/ml anti-streptavidin antibody to a resonator on which streptavidin was immobilized. As expected, we clearly observe the association of anti-streptavidin to the sensor surface proceeding to saturation.

Discussion

As mentioned above, we estimate here the mass sensitivity of the NOSA by growing multiple polyelectrolyte stacks consisting of polyethyleneimine (PEI) and polyacrylic acid (PAA) in a layer by layer manner. Ganesan *et al.*[45] measured the bound mass on a scanning probe cantilever due to the self-assembly of PEI and PAA monolayers. They reported measuring 24 pg of bound mass for a 5 layer polyelectrolyte stack over a surface area of 0.9×10^{-4} cm^2 which corresponded to a bound surface mass density of 2.67×10^{-7} g/cm^2. The functionalized surface area of a single 1-D photonic crystal resonant sensor including the internal surface area of the holes is 8.36 μm^2. Assuming the same surface mass density as above, we calculate the total bound mass on a NOSA sensor for a 5 layer stack of polyelectrolyte monolayers to be 22.3 fg. The corresponding red-shift in the resonant wavelength was observed to be 3.53 nm. The smallest resolvable red-shift can be approximated as the linewidth/50[2] which is approximately 0.01 nm in our system. Thus we estimate the smallest amount of bound mass that can be detected by our current sensor to be 63 ag corresponding to a surface mass coverage of 7.5 pg/mm^2. This value agrees well with our previously estimated mass LOD of the NOSA of tens of attograms[28] using FDTD simulations. Due to the ultra-small mode volume of our 1-D photonic crystal resonator structure we are able to demonstrate a mass LOD that is an improvement on current optical biosensors[17,31,32] which are typically able to achieve mass LODs of a few femtograms. Current progress in improving the Q-factor of such 1-D resonators[46,47] can greatly enhance the detection limit of our devices by orders of magnitude thus paving the way towards the detection of sub- attogram amounts of bound mass.

We compare our sensing platform to another robust, multiplexable photonic crystal based sensing platform developed by Choi *et al.*[18] In their work they report observing a 1 nm red-shift while detecting the association of 500 μg/ml of rabbit IgG (Immunoglobin G). In our experiments, we have used rabbit IgG anti-streptavidin which possesses a similar molecular weight. We have demonstrated an equivalent red-shift of approximately 1 nm for concentrations almost 5 times lower than those presented in reference 18 mentioned above (see Fig. 5).

Recently, researchers have demonstrated high-Q optical resonator sensors with the capability to detect a single biomolecule[3] and virus.[15] In addition other WGM sensors such as capillary based optofluidic ring resonators have demonstrated the ability to detect picomolar concentrations of adsorbed proteins.[48] Our current experiments indicate a higher solution phase detection limit in comparison to these optical sensing techniques. In the case of resonant optical devices, the detection limit is primarily dictated by the Q-factor of the resonators. High Q-factors allow for narrow line-widths which increases the ability to resolve small shifts in the resonant peak. Micro-toroid resonators which possess Q-factors close to 10^8 are capable of resolving resonance shifts as small as 0.001 pm. In comparison our current sensors have a Q-factor of around 3000 thus setting the detection limit to approximately 0.01 nm. However, this is by no means a fundamental limitation of the device architecture. Researchers have recently designed similar 1-D photonic crystal resonators with a theoretical Q-factor as high as 10^8.[47] By incorporating such high-Q 1-D resonators, the NOSA architecture can achieve LODs that are similar to those of state of the art optical biosensors while maintaining a smaller device footprint.

While the detection limit of the current NOSA implementation is lower than some of these other optical interrogation techniques, it is important to note that the refractive index sensitivity (which correlates to the device sensitivity) of 130 nm/RIU of the NOSA[28] is almost an order of magnitude higher than most WGM optical sensors.[49] Fig. 3 shows the electric field distribution within the innermost hole of the 1-D photonic crystal resonator. It is evident that a very significant portion of the resonant optical field exists within the hole thus enabling stronger light-matter interaction at the sensor surface. This enhanced optical interaction leads to a higher device sensitivity in comparison to evanescent field and WGM sensors. Since most antibodies and antigens rarely exceed 20 nm in size they should easily infiltrate the holes of the photonic crystal resonator and bind to the sensor surface.

Another advantage of our approach over other optical resonator designs is its suitability for performing multiplexed detections. Due to the fabrication process and the planar nature of the device, it is easy to fabricate a single bus waveguide coupled to many 1-D photonic crystal resonators for performing multiplexed detections. In contrast, multiplexed detections in microtoroid, microsphere and some microdisk sensors requires complicated alignment of tapered optical fibers in free space[50] thus making these sensors prohibitive for performing highly parallel detections in a robust, integrated sensor platform. Given our observed linewidth and the 100 nm operational range of a standard 1550 nm tunable laser, we expect that 50 1-D resonators could be incorporated along a single waveguide. However with current work on ultra high-Q single-dimensional microcavities[46,47] the number of multiplexed resonators on a single waveguide can easily be extended into the hundreds. Another important advantage of the NOSA design is that the small cavity size results in each resonator possessing a large free spectral range (FSR) of over 200 nm. In comparison, most WGM sensors have cavity lengths over 100 μm resulting in a maximum FSR of 3–5 nm. The large FSR for our NOSA architecture enables each resonator to have a single resonant peak in the output spectrum, thus facilitating interpretation of the multiplexed output signal. The larger FSR of our sensor design also allows for a higher number of resonant sensors to be multiplexed along a waveguide as compared to WGM sensors.

Materials and methods

Fabrication of NOSA device

The NOSA consists of a silicon (Si) waveguide with a 1D photonic crystal micro-cavity that lies adjacent to the waveguide. The side resonator consists of a central defect cavity with 8 holes on either side which form the 1-D photonic crystal. The Si waveguide was designed to be 450 nm wide and 250 nm tall to make it single mode. The low index silicon dioxide (SiO_2) layer which lies beneath the high index Si waveguide helps confine the light within the waveguide core, preventing optical losses into the lower substrate. The devices were fabricated using silicon-on-insulator (SOI) wafers having a device layer thickness of 250 nm which were subsequently patterned using electron beam (e-beam) lithography and finally etched using an inductively coupled plasma etching system. The residual e-beam resist (XR-1541, Dow Corning Corporation) was dissolved in a 100:1 HF solution which is dilute enough to prevent undercutting and releasing the devices from the silica substrate. Lift-off processing was used to mask each resonator on the chip and 1.8 μm of SiO_2 was subsequently evaporated onto the rest of the chip using e-beam evaporation. The evaporated SiO_2 serves two purposes. Firstly, it acts as a vital cladding layer for the nanotapers[51] that is important for coupling light into the end facets of the waveguides and secondly, it protects large portions of the waveguides by masking them and thus preventing degradation in device behavior due to repeated usage. Each waveguide has five evanescently coupled resonators placed adjacent to it where each resonator is designed to have a slightly different cavity spacing. Since the resonant wavelength is dependent on the central cavity length, each resonator has a unique resonant wavelength associated with it.

Experimental setup

The top microfluidic architecture was fabricated from polydimethylsiloxane (PDMS) using a soft lithography technique.[52] After punching inlet and outlet ports, the channels were aligned with the resonators by using a modified overhead optical microscope setup, and secured with a custom plexiglass housing (Figure S3 in ESI†). A laser source (Ando AQ4321D, Ando Corp, San Jose, CA) which is tunable between 1520 nm to 1620 nm was used to excite the waveguides. A lensed fiber is clamped onto a three axis stage and positioned precisely so as to couple light into the nanotaper present at the end facets of the waveguide. The chip is mounted on another 3-axis stage. A lens is used to collect and collimate the light from the output end of the waveguide into a photodetector. A polarizer is placed between the lens and the detector to select only the TE (Transverse Electric) component of light emerging from the waveguide. The photodetector was linked to a PC *via* a GPIB controller (NI GPIB-USB-HS, National Instruments Corp, Austin, TX). A LABVIEW (National Instruments Corp, Austin, TX) script was used for data acquisition. Approximately 750 μW of optical power was launched into the input end of the waveguide and around 10–20 μW of optical power was measured at the output facet of the waveguides.

Surface functionalization

Unless otherwise stated, all chemical reagents were purchased through VWR (West Chester, PA) and Sigma Aldrich (St. Louis, MO) and biological reagents were purchased from United States Biological (Swampscott, MA). After cleaning in piranha solution (1:3 hydrogen peroxide in concentrated sulfuric acid, thirty minutes at 70 °C) sensors were functionalized with 2% aminopropyltrimethoxysilane in 95% ethanol (5% deionized water) for 10 minutes, followed by rinsing in ethanol and curing for two hours at 80 °C. Amine-functionalized sensors were then shaken for two hours in 1 × PBS [1 × PBS is 10 mM phosphate buffer, 137 mM NaCl, and 2.7 mM KCl,], pH 7.4, containing 10 mM glutaraldehyde and 10 mM sodium cyanoborohydride to prepare aldehyde functionalized substrates. Immobilization of the polyelectrolyte multilayer and proteins (described below) was performed in polydimethylsiloxane (PDMS) microfluidic channels, prepared by casting a 1:10 ratio of curing agent to elastomer base over a positive relief master.[52] To refurbish between uses, NOSA devices were soaked in concentrated sulfuric acid overnight to dissolve PDMS residues, after which they were treated for 10 minutes in air plasma (Harrick Plasma Cleaner PDC-32 G, Ithaca, NY), followed by piranha cleaning and functionalization as described above.

Polyelectrolyte multilayer

Deposition of the polyelectrolyte multilayer onto the NOSA sensor was performed in a microfluidic channel (45 mm × 1 mm × 2 cm). After a thirty minute wash in 30 mM sodium citrate buffer, containing 0.1% sodium dodecyl sulfate (SDS) and 0.3 M NaCl, baseline spectra were taken in 1.5 mM sodium citrate buffer, containing 15 mM NaCl. To form the polyelectrolyte multilayer, alternating solutions of polyethylenimine (PEI) and polyacrylic acid (PAA) (2 mg/ml in 1 × PBS) were introduced to the channel for thirty minutes, after which spectra were recorded in 1.5 mM sodium citrate buffer, containing 15 mM NaCl. Covalent cross-linking agents were included during multilayer deposition in order to ensure stability of the polyelectrolyte multilayer to the shear stresses induced by continuous microfluidic flow. Deposition of the initial PEI layer was performed in cyanoborohydride coupling buffer (0.02 M sodium phosphate, pH 7.5, containing 0.2 M sodium chloride and 3.0 g/L sodium cyanoborohydride) and was allowed to conjugate for an hour, and 50 mM 1-ethyl-3-[3-dimethylaminopropyl] carbodiimide (EDC) and 5 mM N-hydroxysuccinimide (NHS) were included in the PAA solution. Ellipsometry (Nanofilm EP3, Nanofilm Technologie GmbH, Göttingen, Germany) was performed on silicon wafers treated in parallel with the NOSA device to quantify thicknesses of deposited multilayers.

Protein immobilization

In order to individually address parallel NOSA resonators, a set of functionalization PDMS microfluidics (5 adjacent channels, each channel 32 μm tall and 42 μm wide) was aligned over APTMS-glutaraldehyde functionalized NOSA sensors for protein immobilization. Of the five parallel NOSA resonators, two were kept as controls and were therefore not further functionalized. Streptavidin hydrazide (100 μg/ml in 1 × PBS, Thermo Fisher Scientific Inc, Rockford, IL) was conjugated to the remaining three resonators for two hours, followed by rinsing in 1 × PBS. Binding kinetics and dynamic range experiments were conducted on streptavidin treated NOSA sensors as described below. For multiplexed interleukin immunoassays, biotinylated monoclonal antibodies to IL-4, IL-6, and IL-8 (100 μg/ml in 1 × PBS) were conjugated for one hour to streptavidin treated NOSA sensors, followed by rinsing in 1 × PBS. After protein immobilization, the functionalization fluidics were removed, and a separate set of detection fluidics (700 μm wide and 32 μm tall) were aligned for the immunoassays described below. The sizes of these channels were selected for experimental convenience and were not optimized for target capture efficiency as described in Squires *et al.*[53] All antibodies and recombinant interleukins were purchased from United States Biological Inc. (Swampscott, Massachusetts) and were used without further purification.

Non-specific blocking

It is often necessary to perform a blocking step prior to performing a biosensing assay in order to prevent non-specific adsorption of analyte and non-target material, and thus improve device sensitivity. Selection of appropriate blocking agents becomes a unique challenge for label-free biosensors that quantify signal based on bound mass, as the sensor cannot distinguish between adsorbed blocking agent and bound analyte. Blocking buffers that have been previously determined to provide high sensitivity and low background noise in ELISA or fluorescence based microfluidic assays may therefore not be suitable for a label-free detection platform, even if the analytes are the same. We have evaluated several blocking agents and determined that 1x PBS containing 0.1% Tween-20 and 0.2 mg/ml bovine albumin (PBST) provides sufficient blocking, without compromising device sensitivity. Data illustrating the effect of blocking buffer on device sensitivity are provided in ESI (Figure S4).†

Immunoassay procedure

After alignment of detection fluidics, remaining aldehydes on the NOSA sensor surface were blocked with 0.1 M Tris, pH 8.0, containing 10 mM sodium cyanoborohydride for at least thirty minutes to prevent non-specific adsorption. The surface was then conditioned in 1 × PBS containing 0.1% Tween-20 and 0.2 mg/ml bovine albumin (PBST), which was also used as the upper cladding fluid during spectral collection. For binding kinetics assays, 10 μg/ml polyclonal anti-streptavidin antibody in PBST was allowed to associate to the immobilized streptavidin for thirty minutes during which output power was collected to determine kinetics of antibody association on the NOSA sensor. Dynamic range of the sensor was determined by associating varying concentrations (0.01 to 500 μg/ml) of polyclonal anti-streptavidin antibody in PBST for 30 minutes, followed by brief rinsing with PBST, and spectral collection. Multiplexed NOSA immunoassays were performed by associating 10 μg/ml of one or multiple recombinant interleukins onto the immobilized monoclonal capture antibodies for 15 minutes, followed by rinsing in PBST, and association of 100 μg/ml secondary polyclonal antibody. Spectra were recorded, and resonant shifts were compared to the baseline spectra. After antibody association, the average resonance shift of control (aldehyde functionalized) resonators was less than 0.01 nm, and the shift of streptavidin functionalized resonators was 0.02 nm. These values correspond to the resolution limit of our sensor, suggesting that the observed shifts in resonance on the antibody functionalized resonators were a result of specific association of target antigens.

Conclusions

In conclusion, we have developed an optofluidic biosensor capable of multiplexed, label-free immunological detection with high device sensitivity and low mass limit of detection. We present a straightforward, repeatable technique to quantify the optical response of the device to changes in bound mass. By measuring device response as a function of growing polyelectrolyte multilayers, we are able to determine sensitivity of 0.35 nm resonance shift per nanometer of surface bound biomolecules. Comparing our results to reports of the mass of grown polyelectrolyte multilayers, we have estimated our device mass limit of detection to be 63 ag and a device sensitivity at least an order of magnitude greater than previously reported devices. Using the streptavidin/anti-streptavidin model, we characterized the dose-response of the NOSA device and observed a dynamic range of 1 to 100 μg/ml. Finally, by monitoring a single resonance during antibody association, we were able to observe binding kinetics in real-time, demonstrating how the NOSA device can be used for *in situ* monitoring of biomolecular interactions.

Acknowledgements

This work was supported by the Nanobiotechnology Center (NBTC), an STC Program of the National Science Foundation under Agreement No. ECS-9876771 and the National Institutes of Health - National Institute of Biomedical Imaging and Bioengineering (NIH-NIBIB) under grant number R21EB007031. Additional support has also been provided by the Defense Advanced Research Projects Agency Microsystems Technology Office (DARPA-MTO) Young Faculty Award Program. Portions of this work were performed at the Cornell Nanoscale Facility, a member of the National Nanotechnology Infrastructure Network, which is supported by the National Science Foundation (Grant ECS-0335765).

References

1 J. N. Anker, W. P. Hall, O. Lyandres, N. C. Shah, J. Zhao and R. P. Van Duyne, *Nat. Mater.*, 2008, **7**, 442–453.
2 S. Arnold, M. Khoshsima, I. Teraoka, S. Holler and F. Vollmer, *Opt. Lett.*, 2003, **28**, 272–274.
3 A. M. Armani, R. P. Kulkarni, S. E. Fraser, R. C. Flagan and K. J. Vahala, *Science*, 2007, **317**, 783–787.
4 J. S. Daniels and N. Pourmand, *Electroanalysis*, 2007, **19**, 1239–1257.
5 R. Raiteri, M. Grattarola, H.-J. Butt and P. Skládal, *Sensors and Actuators B: Chemical*, 2001, **79**, 115–126.
6 M. A. Cooper, *Anal. Bioanal. Chem.*, 2003, **377**, 834–842.
7 R. J. Leatherbarrow and P. R. Edwards, *Curr. Opin. Chem. Biol.*, 1999, **3**, 544–547.
8 G. Canziani, W. T. Zhang, D. Cines, A. Rux, S. Willis, G. Cohen, R. Eisenberg and I. Chaiken, *Methods*, 1999, **19**, 253–269.
9 D. Erickson, S. Mandal, A. H. J. Yang and B. Cordovez, *Microfluidics and Nanofluidics*, 2008, **4**, 33–52.
10 B. Ilic, Y. Yang, K. Aubin, R. Reichenbach, S. Krylov and H. G. Craighead, *Nano Lett.*, 2005, **5**, 925–929.
11 W. U. Wang, C. Chen, K. H. Lin, Y. Fang and C. M. Lieber, *Proceedings of the National Academy of Sciences of the United States of America*, 2005, **102**, 3208–3212.
12 F. Patolsky, G. F. Zheng and C. M. Lieber, *Analytical Chemistry*, 2006, **78**, 4260–4269.
13 A. Ymeti, J. Greve, P. V. Lambeck, T. Wink, S. van Hovell, T. A. M. Beumer, R. R. Wijn, R. G. Heideman, V. Subramaniam and J. S. Kanger, *Nano Lett.*, 2007, **7**, 394–397.
14 A. Brandenburg, *Sensors and Actuators B-Chemical*, 1997, **39**, 266–271.
15 F. Vollmer, S. Arnold and D. Keng, *Proceedings of the National Academy of Sciences*, 2008, **105**, 20701–20704.
16 H. Y. Zhu, I. M. White, J. D. Suter, M. Zourob and X. D. Fan, *Anal. Chem.*, 2007, **79**, 930–937.
17 M. R. Lee and P. M. Fauchet, *Opt. Express*, 2007, **15**, 4530–4535.
18 C. J. Choi and B. T. Cunningham, *Lab Chip*, 2007, **7**, 550–556.
19 B. Schmidt, V. Almeida, C. Manolatou, S. Preble and M. Lipson, *Appl. Phys. Lett.*, 2004, **85**, 4854–4856.
20 A. W. Wark, H. J. Lee and R. M. Corn, *Anal. Chem.*, 2005, **77**, 3904–3907.
21 C.-Y. Yang, E. Brooks, Y. Li, P. Denny, C.-M. Ho, F. Qi, W. Shi, L. Wolinsky, B. Wu, D. T. W. Wong and C. D. Montemagno, *Lab Chip*, 2005, **5**, 1017–1023.
22 J. Homola, *Chemical Reviews*, 2008, **108**, 462–493.
23 J. T. Robinson, L. Chen and M. Lipson, *Opt. Express*, 2008, **16**, 4296–4301.
24 D. K. Armani, T. J. Kippenberg, S. M. Spillane and K. J. Vahala, *Nature*, 2003, **421**, 925–928.
25 F. Vollmer, D. Braun, A. Libchaber, M. Khoshsima, I. Teraoka and S. Arnold, *Appl. Phys. Lett.*, 2002, **80**, 4057–4059.
26 A. Ksendzov and Y. Lin, *Opt. Lett.*, 2005, **30**, 3344–3346.
27 C. Sang-Yeon and N. M. Jokerst, *Photonics Technology Letters, IEEE*, 2006, **18**, 2096–2098.
28 S. Mandal and D. Erickson, *Opt. Express*, 2008, **16**, 1623–1631.
29 Y. Akahane, T. Asano, B.-S. Song and S. Noda, *Nature*, 2003, **425**, 944–947.
30 B.-S. Song, S. Noda, T. Asano and Y. Akahane, *Nat. Mater.*, 2005, **4**, 207–210.
31 K. De Vos, I. Bartolozzi, E. Schacht, P. Bienstman and R. Baets, *Opt. Express*, 2007, **15**, 7610–7615.
32 H. Zhu, I. M. White, J. D. Suter, P. S. Dale and X. Fan, *Opt. Express*, 2007, **15**, 9139–9146.
33 C. Monat, P. Domachuk and B. J. Eggleton, *Nat. Photonics*, 2007, **1**, 106–114.
34 D. Psaltis, S. R. Quake and C. H. Yang, *Nature*, 2006, **442**, 381–386.
35 J. S. Foresi, P. R. Villeneuve, J. Ferrera, E. R. Thoen, G. Steinmeyer, S. Fan, J. D. Joannopoulos, L. C. Kimerling, H. I. Smith and E. P. Ippen, *Nature*, 1997, **390**, 143–145.
36 M. Polanski and N. L. Anderson, *Biomarker Insights*, 2007, **1**, 1–48.
37 T. Bachelot, I. Ray-Coquard, C. Menetrier-Caux, M. Rastkha, A. Duc and J. Y. Blay, *Br. J. Cancer*, 88, pp. 1721–1726.
38 Z. Chen, P. S. Malhotra, G. R. Thomas, P. G. Ondrey, D. C. Duffey, C. W. Smith, N. Enamorado, N. T. Yeh, G. S. Kroog, S. Rudy, L. McCullagh, S. Mousa, M. Quezado, L. L. Herscher and C. Van Waes, *Clinical Cancer Research*, 1999, **5**, 1369–1379.
39 S. X. Leng, J. E. McElhaney, J. D. Walston, D. Xie, N. S. Fedarko and G. A. Kuchel, *J Gerontol A Biol Sci Med Sci*, 2008, **63**, 879–884.
40 A. J. A. Lambeck, A. P. G. Crijns, N. Leffers, W. J. Sluiter, K. A. ten Hoor, M. Braid, A. G. J. van der Zee, T. Daemen, H. W. Nijman and W. M. Kast, *Clin Cancer Res*, 2007, **13**, 2385–2391.
41 P. John V, *Ann. N.Y. Acad. Sci.*, 1993, **694**, 216–233.
42 A. DeLean, P. J. Munson and D. Rodbard, *Am J Physiol Endocrinol Metab*, 1978, **235**, E97–102.
43 O. A. Saleh and L. L. Sohn, *Proc. Natl. Acad. Sci. USA*, 2003, **100**, 820–824.
44 H. Y. Zhu, I. M. White, J. D. Suter, M. Zourob and X. D. Fan, *Analyst*, 2008, **133**, 356–360.
45 P. G. Ganesan, X. Wang and O. Nalamasu, *Appl. Phys. Lett.*, 2006, **89**, 213107–213113.
46 C. Sauvan, G. Lecamp, P. Lalanne and J. Hugonin, *Opt. Express*, 2005, **13**, 245–255.
47 M. Notomi, E. Kuramochi and H. Taniyama, *Opt. Express*, 2008, **16**, 11095–11102.

48 J. D. Suter, I. M. White, H. Zhu, H. Shi, C. W. Caldwell and X. Fan, *Biosens. Bioelectron.*, 2008, **23**, 1003–1009.
49 I. M. White, H. Oveys, X. Fan, T. L. Smith and J. Zhang, *Appl. Phys. Lett.*, 2006, **89**, 191106–191113.
50 F. Vollmer, S. Arnold, D. Braun, I. Teraoka and A. Libchaber, *Biophys. J.*, 2003, **85**, 1974–1979.
51 V. R. Almeida, R. R. Panepucci and M. Lipson, *Opt. Lett.*, 2003, **28**, 1302–1304.
52 D. C. Duffy, J. C. McDonald, O. J. A. Schueller and G. M. Whitesides, *Anal. Chem.*, 1998, **70**, 4974–4984.
53 T. M. Squires, R. J. Messinger and S. R. Manalis, *Nat Biotech*, 2008, **26**, 417–426.